The Astrophysical Journal, 944:162 (14pp), 2023 February 20 https://doi.org/10.3847/1538-4357/acaaa6

The ESO-VLT MIKiS Survey Reloaded: Exploring the Internal Kinematics of NGC 6440*

Silvia Leanza[1,2], Cristina Pallanca[1,2], Francesco R. Ferraro[1,2], Barbara Lanzoni[1,2], Emanuele Dalessandro[2], Mario Cadelano[1,2], Enrico Vesperini[3], Livia Origlia[2], Alessio Mucciarelli[1,2], and Elena Valenti[4,5]
[1] Dipartimento di Fisica e Astronomia, Università di Bologna, Via Gobetti 93/2 I-40129 Bologna, Italy; silvia.leanza2@unibo.it
[2] INAF-Osservatorio di Astrofisica e Scienze dello Spazio di Bologna, Via Gobetti 93/3 I-40129 Bologna, Italy
[3] Department of Astronomy, Indiana University, Bloomington, IN 47401, USA
[4] European Southern Observatory, Karl-Schwarzschild-Strasse 2, D-85748 Garching bei Munchen, Germany
[5] Excellence Cluster ORIGINS, Boltzmann-Strasse 2, D-85748 Garching Bei Munchen, Germany
Received 2022 September 28; revised 2022 December 1; accepted 2022 December 9; published 2023 February 22

Abstract

In the context of the ESO-VLT Multi-Instrument Kinematic Survey of Galactic globular clusters, here we present the line-of-sight velocity dispersion profile of NGC 6440, a massive globular cluster located in the Galactic bulge. By combining the data acquired with four different spectrographs, we obtained the radial velocity of a sample of ∼1800 individual stars distributed over the entire cluster extension, from ∼0.″1 to 778″ from the center. Using a properly selected sample of member stars with the most reliable radial velocity measures, we derived the velocity dispersion profile up to 250″ from the center. The profile is well described by the same King model that best fits the projected star density distribution, with a constant inner plateau (at $\sigma_0 \sim 12$ km s^{-1}) and no evidence of a central cusp or other significant deviations. Our data allowed us to study the presence of rotation only in the innermost regions of the cluster ($r < 5''$), revealing a well-defined pattern of ordered rotation with a position angle of the rotation axis of ∼132° ± 2° and an amplitude of ∼3 km s^{-1} (corresponding to $V_{\rm rot}/\sigma_0 \sim 0.3$). In addition, a flattening of the system qualitatively consistent with the rotation signal has been detected in the central region.

Unified Astronomy Thesaurus concepts: Globular star clusters (656); Stellar kinematics (1608); Spectroscopy (1558)

1. Introduction

The ESO-VLT Multi-Instrument Kinematic Survey (MIKiS; Ferraro et al. 2018b, 2018c) has been specifically designed to characterize the kinematical properties of a representative sample of Galactic globular clusters (GGCs) in different dynamical evolutionary stages. The approach proposed in MIKiS is to derive both the velocity dispersion and the rotation profiles from the line-of-sight velocities of a statistically significant sample of individual stars distributed over the entire radial extension of each investigated stellar system. To this end, the spectroscopic capabilities of different instruments located at the ESO Very Large Telescope (VLT) are used: the survey was designed to take advantage of the adaptive optics (AO) assisted integral field spectrograph SINFONI, the multiobject integral field spectrograph KMOS, and the multiobject fiber-fed spectrograph FLAMES/GIRAFFE, and it has been recently complemented with a series of specific proposals and an ongoing Large Program (106.21N5, PI: Ferraro) that exploits the remarkable performance of the AO-assisted integral field spectrograph MUSE.

In particular, the powerful combination of the two AO-assisted integral field spectrographs SINFONI and MUSE allows an unprecedented exploration of the kinematics of the innermost GGC core regions, reaching a spatial resolution comparable to that obtained from Hubble Space Telescope (HST) observations. Indeed, the central portions of collisional stellar systems like the GGCs are the most intriguing regions where recurrent stellar interactions are expected to generate exotic objects, like interacting binaries, blue stragglers, and millisecond pulsars (Bailyn 1995; Pooley et al. 2003; Ransom et al. 2005; Ferraro et al. 2018a). Moreover, even the long-sought intermediate-mass black holes (IMBHs; e.g., Portegies Zwart et al. 2004; Giersz et al. 2015) might populate the central regions of GCs according to the extrapolation of the "Magorrian relation" (Magorrian et al. 1998).

MIKiS is part of a long-term project (Cosmic-Lab) aimed at performing a comprehensive study of a sample of representative GGCs. Thus, the kinematical information provided by MIKiS is combined with additional key properties of each system derived from complementary observations as (1) plane-of-the-sky kinematics obtained from the stellar proper motions (PMs) measured with HST and Gaia (see, e.g., Raso et al. 2020; Leanza et al. 2022); (2) updated structural parameters obtained from high-quality density profiles derived from star counts, instead of surface brightness (e.g., Lanzoni et al. 2007, 2010; Miocchi et al. 2013; Lanzoni et al. 2019; Cadelano et al. 2020a; Pallanca et al. 2021); and (3) properties of the populations of stellar exotica (Pallanca et al. 2010, 2013, 2014; Ferraro et al. 2015, 2016; Cadelano et al. 2017a, 2017b; Pallanca et al. 2017; Cadelano et al. 2018, 2019, 2020b) and their connection with the dynamical evolution of the parent cluster (see Ferraro et al. 2009a, 2012; Lanzoni et al. 2016; Ferraro et al. 2018b, 2019; Dalessandro et al. 2019). In principle, this approach can provide the full characterization of the investigated stellar systems.

* Based on observations collected at the European Southern Observatory, Cerro Paranal (Chile), under proposal 193.D-0232 (PI: Ferraro), 195.D-0750 (PI: Ferraro), 60.A-9489 (PI: Ferraro), and 093.D-0319 (PI: Lanzoni).

In this paper, we present the velocity dispersion profile and the detection of internal rotation for NGC 6440, a massive, metal-rich ([Fe/H] ~ -0.56; Origlia et al. 1997, 2008), and highly extincted ($E(B-V)=1.15$; Valenti et al. 2004, 2007; see also Pallanca et al. 2019) GC, located in the Milky Way bulge, 1.3 kpc away from the center of the Galaxy (Harris 1996). This system has been subject to a detailed analysis by our group because it was suspected (Mauro et al. 2012) to have properties similar to those detected in Terzan 5 and Liller 1, two massive clusters in the bulge direction that are suspected to be the relics of the primordial assembling process of the Galactic bulge and define a new class of stellar systems named "Bulge Fossil Fragments" (see Ferraro et al. 2009b, 2016, 2021). Those studies allowed us to redetermine with an improved level of accuracy the overall characteristics of NGC 6440, thus redesigning a sort of new identity card of the cluster. A high-resolution extinction map has been obtained (see Pallanca et al. 2019) and used to correct the effects of the strong differential reddening in the direction of the cluster. This allowed us to derive a high-precision, differential-reddening-corrected, PM-selected color–magnitude diagram (CMD), from which a new determination of the cluster age has been obtained (see Pallanca et al. 2021). This data set has also been used to derive an accurate star density profile from which new structural parameters and characteristic relaxation times have been derived (see Pallanca et al. 2021). With regard to the study of the exotic populations, we provided the identification of the optical companion to an accreting millisecond X-ray pulsar (see Cadelano et al. 2017a).

The present paper is organized as follows. In Section 2 we present the observations and describe the procedures performed for the data reduction. In Section 3 we discuss the selection of the samples, the methods to determine the radial velocities (RVs), and the strategy adopted to homogenize the different data sets available. The results are presented in Section 4, while Section 5 is devoted to the discussion and conclusions.

2. Observations and Data Reduction

To characterize the internal kinematics of NGC 6440, we measured the RVs of resolved, individual stars distributed over the entire radial extension of the system by using a multi-instrument approach.

1. *MUSE.*—The spectra of the stars in the innermost cluster regions were acquired with the AO-assisted integral field spectrograph MUSE in the Narrow Field Mode (NFM) configuration (Bacon et al. 2010), as part of the NFM science verification run (program ID: 60.A-9489(A); PI: Ferraro; see Table 1). MUSE is located on the Yepun (VLT-UT4) telescope at the ESO Paranal Observatory. It consists of 24 identical integral field units (IFUs), and it is available in two configurations, Wide Field Mode (WFM) and NFM, the latter providing a higher spatial resolution. MUSE/NFM is equipped with the GALACSI-AO module (Arsenault et al. 2008; Ströbele et al. 2012) and covers a $7\farcs5 \times 7\farcs5$ field of view with a spatial sampling of $0\farcs025$ pixel^{-1}. The spectral range samples from 4800 to 9300 Å with a resolving power $R \sim 3000$ at $\lambda \sim 8700$ Å. Our MUSE data set consists of a mosaic of four MUSE/NFM pointings centered within $15''$ from the cluster center (Pallanca et al. 2021). For each pointing, multiple exposures, usually three, were acquired with a small dithering pattern and a rotation offset of 90° between consecutive exposures, in order to remove possible systematic effects and resolution differences between the individual IFUs. Each exposure has been acquired with an exposure time of 850 s, and the DIMM seeing during the observations ranged from $0\farcs45$ to $0\farcs8$. The MUSE/NFM data set was reduced by using the standard MUSE pipeline (Weilbacher et al. 2020). In a first step, the pipeline applies the bias subtraction, flat-fielding, and wavelength calibration for each individual IFU, and, in a second step, it uses these preprocessed data of each IFU to perform the sky subtraction and flux and astrometric calibration. In addition, all the data are corrected for the heliocentric velocity. Then, the data

Table 1
Spectroscopic Data Sets for NGC 6440

Name	Date	$N_{\rm exp}$	$t_{\rm exp}$ (s)
	MUSE/NFM		
C	2018-9-14	3	850
E	2018-9-14	3	850
N	2018-9-12	3	850
S	2018-9-13	2	850
	SINFONI		
HR	2014-8-16	5	20
LRNE	2014-8-14	5	20
LRSE	2014-8-14	4	20
HRC	2015-6-24	6	30
	2016-7-21	6	30
HRE	2015-6-25	6	20
	2016-7-29	6	20
LRE	2016-7-30	6	30
LRN	2016-6-30	6	30
LRS	2016-7-30	6	30
LRSW	2015-7-17	6	30
LRW	2016-7-29	6	30
	KMOS		
kmos_1	2014-5-10	3	30
kmos_2	2014-7-13	3	30
kmos_3	2014-7-04	3	30
kmos_4	2014-7-13	3	30
kmos_5	2014-7-13	3	30
kmos_6	2014-7-13	3	30
kmos_7	2014-7-13	3	30
kmos_8	2014-7-13	3	30
kmos_9	2014-7-13	3	30
kmos_10	2014-7-13	3	30
kmos_external_1	2014-7-20	3	30
kmos_external_2	2014-7-20	3	30
	FLAMES		
flames_1	2014-6-19	2	2700
flames_2	2014-6-20/23	2	2700
flames_3	2014-6-23/2014-7-08	2	2700
flames_alt_1	2014-7-08	2	2700
flames_alt_2	2014-7-08	2	2700

Note. Name, observation date, number of exposures ($N_{\rm exp}$), and exposure time ($t_{\rm exp}$, in seconds) of each exposure for the MUSE/NFM, SINFONI, KMOS, and FLAMES pointings analyzed in this paper. In the name of the SINFONI pointings, LR and HR indicate the two different instrument configurations used here (low and high resolution, respectively).

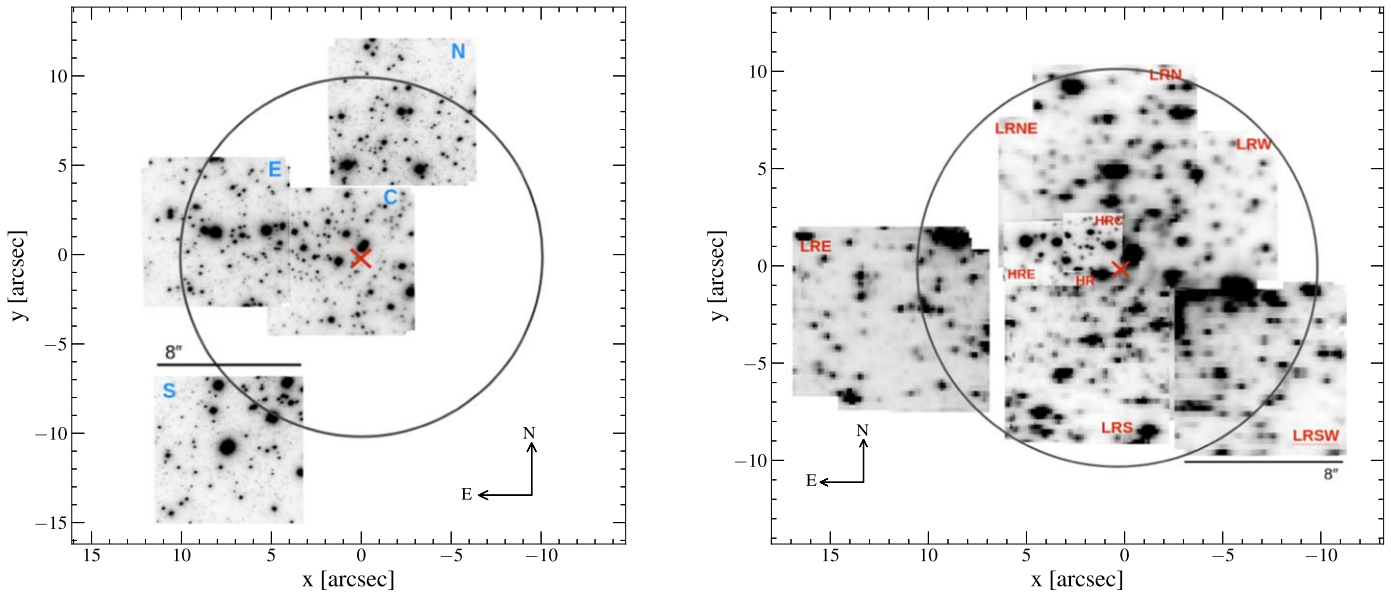

Figure 1. Left: reconstructed *I*-band images of the MUSE/NFM pointings. The circle is centered on the cluster center (red cross, from Pallanca et al. 2021) and has a radius of 10′. Right: reconstructed mosaic of the SINFONI/LR fields (each sampling 8″ × 8″ on the sky) and SINFONI/HR pointings (with a 3″ × 3″ field of view). The red cross and the circle are as in the left panel. In both panels the names of the pointings are labeled.

from all 24 IFUs are combined into a single data cube. As the last step, the pipeline provides a final data cube by combining the data cubes of the multiple exposures of each pointing, taking into account the offsets and rotations among the different exposures. The mosaic of the reconstructed *I*-band images from the stacking of MUSE data cubes is shown in the left panel of Figure 1. Each pointing is labeled with a name according to its position with respect to the cluster center ("C," "S," "E," and "N" standing for central, southern, eastern, and northern pointing, respectively).

2. *SINFONI*.—The MUSE/NFM data analysis in the innermost cluster regions has been complemented using additional AO-assisted integral field observations, performed with the spectrograph SINFONI (Eisenhauer et al. 2003) at the ESO-VLT, in the near-infrared range 1.1–2.45 μm. The observations were conducted under ESO proposals 093.D-0319(A) (PI: Lanzoni) and ID:195.D-0750(A) (PI: Ferraro) (see Table 1), by using the *K*-band grating, providing a spectral resolution $R \sim 4000$ and sampling the 1.95–2.45 μm wavelength range. The data set covers a region within $\sim$16″ from the cluster center and consists of seven pointings acquired by adopting the spatial scale of 0.″25 spaxel^{-1} corresponding to a field of view of 8″ × 8″ (hereafter "LR" for low resolution) and three pointings with the spatial scale of 0.″1 spaxel^{-1} and a 3″ × 3″ field of view (hereafter "HR" for high resolution). Multiple exposures (usually 6 for the LR pointings and 12 for the HR fields) of 20–30 s each were performed on the target and, for background subtraction purposes, on a sky position located $\sim$165″ from the center, following the target-sky sky-target sequence. The observations have been executed under an average DIMM seeing of $\sim$0.″8, leading to a Strehl ratio between 10 and 40. The data reduction was performed by using esorex (3.13.6) following the workflow 3.3.2 under the EsoReflex environment (Freudling et al. 2013). The pipeline first corrects all target and sky exposures for darks, flats, geometrical distortions, and differential atmospheric refraction. Then, the sky background is subtracted by using the sky exposures, the wavelength calibration is performed through the observations of a Th-Ar reference arc lamp, and the data cubes are built for each exposure by combining the corrected target frames. The right panel of Figure 1 shows the reconstructed image of the SINFONI pointings obtained by stacking the data cubes in the wavelength range 2.15–2.18 μm. Clearly, some stars are in common with the MUSE data set, but the SINFONI pointings, in spite of a worse angular resolution, also sample the west and southwest regions around the cluster center that remained uncovered by MUSE (see Figure 2). In Figure 3 we compare the same cluster region as seen in the reconstructed MUSE and SINFONI images (middle and right panels, respectively) and in the HST observations (left panels). This well illustrates the exceptional resolving capabilities of the AO systems used in the SINFONI (especially in the HR setup) and, even more, in the MUSE observations, which are mandatory to obtain large samples of RVs of individual stars in the high-density core of dense stellar systems like NGC 6440.

3. *KMOS*.—To investigate the cluster kinematics at intermediate distances from the center, we have used the integral field spectrograph KMOS (Sharples et al. 2013) at ESO-VLT, which is equipped with 24 IFUs that can be allocated within a 7.′2-diameter field of view. Each IFU covers a projected area on the sky of about 2.″8 × 2.″8, with a spatial sampling of 0.″2 pixel^{-1}. We have used the YJ grating covering the 1.025–1.344 μm spectral range at a resolution $R \sim 3400$, corresponding to a spectral sampling of $\sim$1.75 Å pixel^{-1}. The data have been collected as part of the ESO Large Program ID: 193.D-0232(A). These consist of 12 pointings within $\sim$6′ from center, each one obtained with three subexposures 30 s long. Every IFU is typically centered on one star, selected at $J < 14$ along the red giant branch (RGB) of the cluster

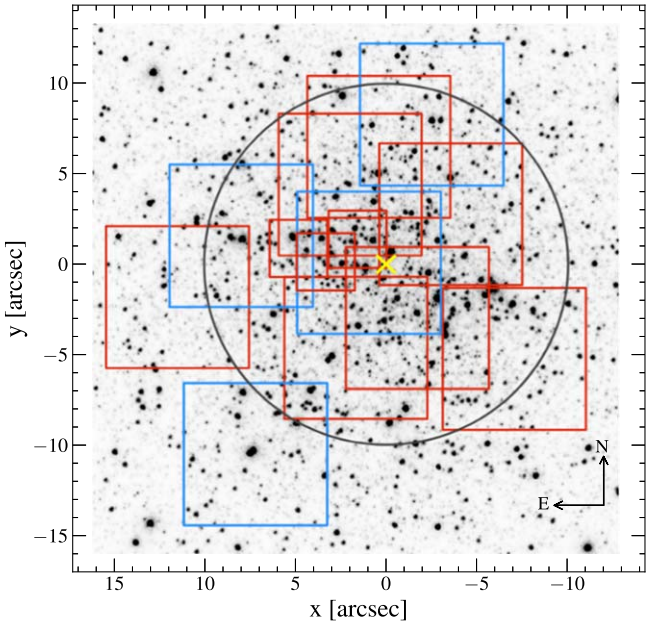

Figure 2. HST/WFC3 image of the central region of NGC 6440 with the areas sampled by the spectroscopic observations overplotted: the blue squares show the fields of the four MUSE/NFM pointings (∼8″ × 8″ on the sky), the large red squares are the SINFONI/LR fields (∼8″ × 8″), and the small red squares are the SINFONI/HR pointings (∼3″ × 3″). The black circle has a radius of 10″ and is centered on the cluster center (yellow cross, from Pallanca et al. 2021).

from the near-infrared SOFI catalog, available at http://www.bo.astro.it/~GC/ir_archive/ (Valenti et al. 2004, 2007), and a Two Micron All Sky Survey (2MASS) catalog in the J, H, and K_s filters sampling the outer regions. The KMOS data reduction has been performed by using the dedicated pipeline[6] executing background subtraction, flat-field correction, and wavelength calibration.

4. *FLAMES*.—The external regions of NGC 6440 have been sampled out to ∼12′ from the center by using the fiber-fed multiobject spectrograph FLAMES (Pasquini et al. 2002) in the GIRAFFE/MEDUSA mode. This configuration consists of 132 fibers, each one with an aperture of 1.″2 on the sky, that can be allocated over a field of view of 25′ in diameter. As for KMOS, also the FLAMES observations have been performed within MIKiS under the ESO Large Program 193.D-0232(B). The spectra were acquired with the HR21 grating setup, which provides a resolving power $R \sim 18{,}000$ between 8484 and 9001 Å. Five pointings have been performed, each one securing two exposures of 2700 s. The targets are RGB stars brighter than $J = 14$ selected from the same photometric SOFI catalog used for the KMOS targets and from the 2MASS catalog. The data set has been reduced with the dedicated ESO pipelines (see footnote 1), including bias subtraction, flat-fielding correction, wavelength calibration, and extraction of one-dimensional spectra. For each spectrum, the sky background has been subtracted, using a master sky spectrum obtained from the sky exposures acquired with 15–20 dedicated fibers in each pointing.

[6] http://www.eso.org/sci/software/pipelines/

3. Analysis

To properly analyze the four data sets, each one acquired with a different instrument, we have performed specific analyses. They are fully described in dedicated papers and briefly summarized below.

3.1. MUSE/NFM Data Set

For the extraction of the spectra from the MUSE/NFM data cubes we used the code PampelMuse presented in Kamann et al. (2013). This is software dedicated to the extraction of individual stellar spectra from MUSE data in crowded regions of the sky, such as GC cores, by performing a source deblending via wavelength-dependent point-spread function (PSF) fitting. While all the details can be found in Kamann et al. (2013), in the following we briefly describe the main steps of the procedure.

Besides the spectroscopic data cube, PamelMuse needs as input a photometric reference catalog providing the coordinates and magnitudes of all the stars across the field of view. To ensure high photometric completeness and astrometric accuracy, we have used the HST/WFC3 catalog presented in Pallanca et al. (2021), and to properly include also the brightest stars ($I < 16$), which are saturated in those long exposures used to build the catalog above, we analyzed the HST/WFC3 images acquired under the proposal GO15232 in the F555W and F814W filters (hereafter V and I, respectively). The photometric analysis of this data set has been performed following the procedures described in Anderson & King (2006), using the publicly available program img2xym)_WFC.09x10. To place the instrumental coordinates onto the absolute astrometric system, and to calibrate the instrumental magnitudes, we have used the stars in common with the catalog of Pallanca et al. (2021). For source deblending purposes, PampelMuse also needs in input an analytical PSF model. We thus selected the MAOPPY function (Fétick et al. 2019), which is already implemented in the code (see Gottgens et al. 2021) and is designed to accurately reproduce the typical double-component (core and halo) shape of the AO-corrected PSF in MUSE/NFM observations. Once setting the inputs, the spectra are extracted from the observed data cubes through subsequent steps. First, a subsample of isolated stars, on which the PSF will be modeled, is selected according to several criteria, including signal-to-noise ratio (S/N) higher than a certain threshold ($S/N > 5$), relative contribution from neighboring sources negligible in the region where the PSF is modeled, and no bright stars within a distance equal to 1.5× the PSF definition radius. The S/N is mainly estimated from the magnitudes in the input catalog and an initial guess on the PSF parameters. In the second step, the PSF-fitting procedure is applied to the selected subsample of stars in each individual slice of the data cube, providing, as output, the wavelength dependencies of the PSF parameters and of the source coordinates. Finally, these wavelength dependencies are adopted in the PSF-fitting procedure that is performed through the slices of the data cube, to extract the spectra of all the sources present in the MUSE field of view. Among all the extracted spectra, we selected only those marked as "good" by PampelMuse, which correspond to individual stars with $S/N \geqslant 10$.

The RVs of the target stars have been measured from the Doppler shifts of the Calcium triplet lines in the wavelength

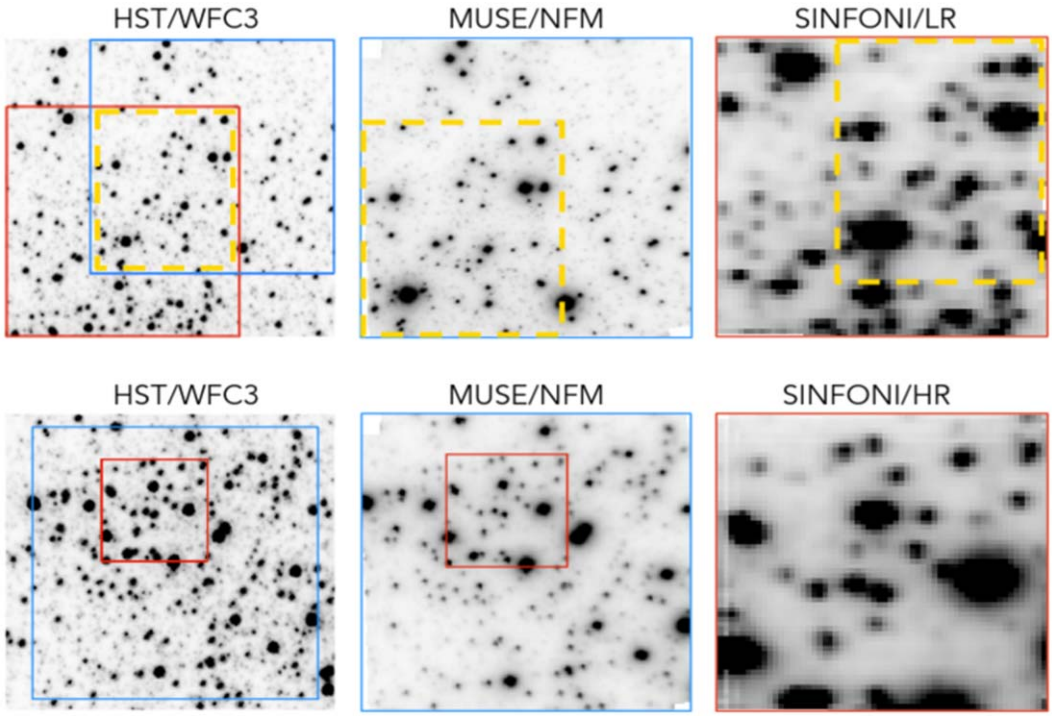

Figure 3. Top panels: comparison among the HST/WFC3 image (left panel), the reconstructed *I*-band image of a MUSE/NFM pointing (middle panel), and the stack image of a SINFONI/LR pointing (right panel), of a central area of NGC 6440. In the left panel, the blue square marks the MUSE/NFM field of view ($\sim 8'' \times 8''$ on the sky), as in the middle panel, and the red region indicates the SINFONI/LR pointing ($\sim 8'' \times 8''$) shown in the left panel, while, in all the panels, the yellow dashed lines mark the common area among the three images. Bottom panels: comparison among the images of the same area of the cluster (bounded by the red square, $\sim 3'' \times 3''$ on the sky) obtained using HST/WFC3 (left), MUSE/NFM (middle), and the stack image of a SINFONI/HR pointing (right). The blue square in the left panel marks the area of the MUSE/NFM field ($\sim 8'' \times 8''$ on the sky) shown in the middle panel.

range 8450–8750 Å. To this end, the extracted spectra have been normalized to the continuum (estimated through a spline fitting in the 7300–9300 Å range). Then, a library of template synthetic spectra has been computed with the SYNTHE code (Sbordone et al. 2004 and Kurucz 2005), assuming an α-enhanced chemical mixture and the cluster metallicity ([α/Fe] = 0.34 dex and [Fe/H] = −0.56 dex; Origlia et al. 2008) and adopting a set of atmospheric parameters (effective temperature and gravity) appropriate for the evolutionary stage of the target stars, as derived from the CMD. The template spectra have been convolved with a Gaussian profile to reproduce the spectral resolution of MUSE and resampled at the same pixel size of the observed spectra. The procedure adopted to measure the target RV computes the residuals between the observation and each template spectrum of the library shifted in velocity in steps of 0.1 km s^{-1}. The distribution of the residuals showing the smallest standard deviation ($\sigma_{\rm min}$) provides the best-fit synthetic spectrum (and hence the best estimate of the stellar atmospheric parameters), and from the minimum of this distribution the RV of the target is derived. A value of S/N independent of that obtained by PampelMuse has been computed for each spectrum as the ratio between the average of the counts and their standard deviation in the wavelength range 8000–9000 Å. We will use this S/N estimate in the following analysis.

The uncertainties on the RV measures have been estimated by means of Monte Carlo simulations. By adding different amounts of Poisson noise to the adopted synthetic templates, we simulated ∼9000 observed spectra with S/Ns ranging from 10 to 90, in steps of 10, running 100 simulations for every considered value of S/N. Then, this sample has been analyzed as for real observations, computing the residuals between the simulations and each synthetic spectrum of the library progressively shifted in velocity, as described above. For each synthetic spectrum we selected the distribution of residuals showing the smallest standard deviation ($\sigma_{\rm min}$) and adopted the corresponding value of RV. This allowed us to plot the difference between the output and the input RVs (ΔRV) as a function of $\sigma_{\rm min}$, from which a polynomial relation between the two parameters has been obtained, with the values of ΔRV increasing for increasing $\sigma_{\rm min}$ (and hence for decreasing S/Ns). Finally, knowing the value of $\sigma_{\rm min}$ of the observed spectra, we used this relation to determine the corresponding value of ΔRV, which has been adopted as RV uncertainty. The typical RV errors are ∼2 km s^{-1} for the brightest stars ($I < 16$), and they increase up to ∼8 km s^{-1} for the faintest targets, as shown in the top left panel of Figure 4. To check that the measured RVs were homogeneous among the different MUSE pointings, we compared the values obtained for the stars in common between the two overlapping fields (the central and the east ones) and the average RV value obtained in each pointing, always finding a good agreement within the errors. In the case of multiple exposures for the same star, we adopted as the final RV the weighted mean of all the measures, by using the individual errors as weights.

The final MUSE catalog consists of 1128 individual RV measures for stars located between ∼0.″1 and ∼18″ from the cluster center, in the magnitude range $13 < I < 22$ (see Table 2). The position of the stars on the plane of the sky is shown in the right panel of Figure 5 (blue triangles), while the first panel on the left of Figure 6 shows the corresponding CMD.

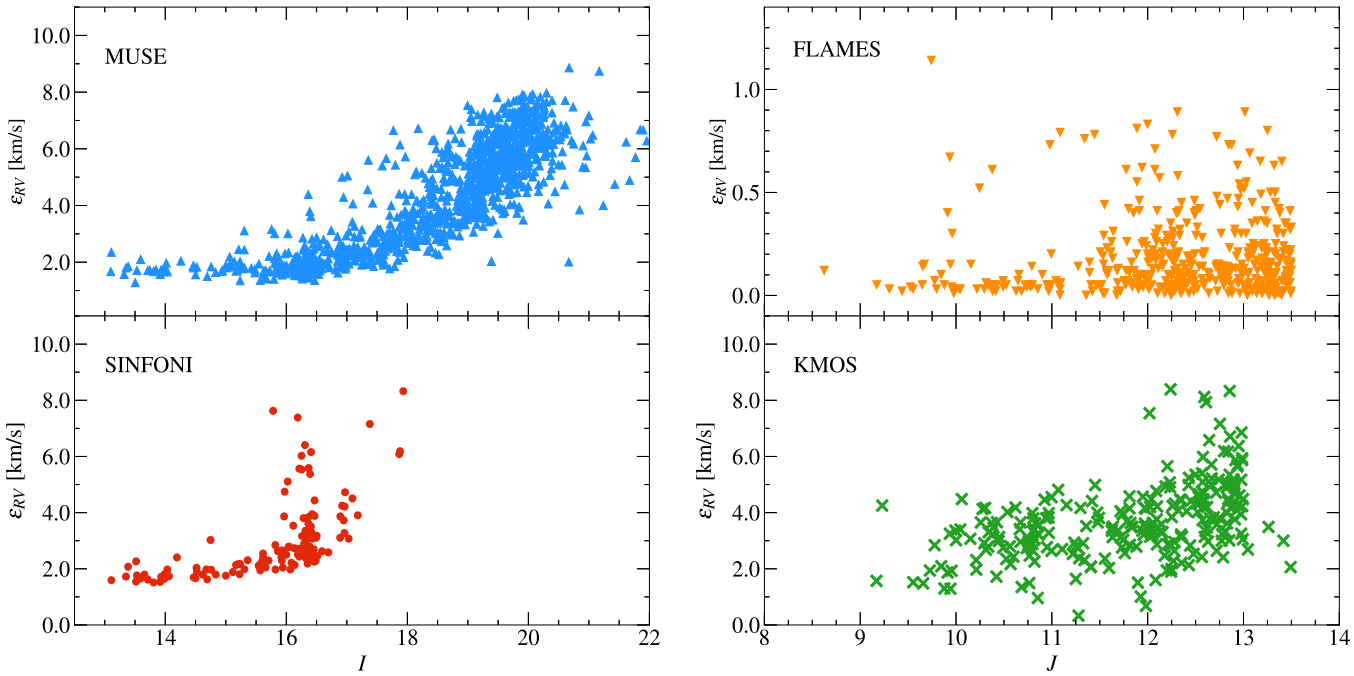

Figure 4. RV uncertainty (ϵ_{RV}) as a function of the star magnitude for the observed targets in the MUSE/NFM, SINFONI, FLAMES, and KMOS samples (top left, bottom left, top right, and bottom right panels, respectively; see labels).

Table 2
Summary of the Different Data Sets Used in This Work

Data Set	Number of Stars	Radial Region in Arcseconds	Magnitude Range
MUSE/NFM	1128	0.1–18.0	$13.0 < I < 22.0$
SINFONI	138	1.1–15.0	$13.0 < I < 18.0$
KMOS	258	1.1–407.3	$9.2 < J < 13.5$
FLAMES	448	22.0–778.5	$8.6 < J < 13.5$

Note. For each data set, the columns list the name of the instrument, the number of stars with RV measured, the sampled radial region expressed as the distance from the center in arcseconds, and the magnitude range of the target stars.

3.2. SINFONI Data Set

A forthcoming paper (C. Pallanca et al. 2023, in preparation) will be specifically devoted to the detailed description of the procedure adopted for the analysis of the SINFONI spectra. Here we just summarize the main key points.

First of all, in each observed data cube, we selected all the spaxels with photon counts above a threshold of 10σ the background level. Setting the threshold level to such a high value guarantees the selection of only the spaxels acquired at the largest S/N. A value of RV has been measured from the 1D spectrum extracted from each selected spaxel, applying a procedure analogous to that adopted for the MUSE/NFM data, using the Doppler shift of the $^{12}C^{16}O$ band heads, instead of the Calcium triplet lines. More specifically, the observed spectra have been compared with synthetic templates progressively shifted in velocity, computed with the SYNTHE code (Sbordone et al. 2004; Kurucz 2005) in the appropriate near-IR wavelength range and at the SINFONI spectral resolution. We used synthetic spectra computed for 10 pairs of effective temperature and surface gravity properly sampling the entire RGB of the cluster, with iron and α-element abundances measured by Origlia et al. (2008), plus seven additional models with appropriate carbon-depletion [C/Fe] = −0.36 dex (Origlia et al. 2008) for stars above the RGB bump. This is to take into account the fact that the deepness of the CO band heads depends on both the temperature and the chemical abundance, and the stars above the RGB bump could be depleted in carbon. The best estimates of the RV and its uncertainty have been evaluated as in the case of the MUSE data, from the distribution of the residuals between the observed and the synthetic spectra showing the smallest standard deviation and from Monte Carlo simulations, respectively. The RV errors are of the order of 2 km s^{-1}, and their trend as a function of the star magnitude is shown in the bottom left panel of Figure 4.

From the cross-correlation with the HST catalog described above we finally identified the resolved stars in each SINFONI data cube. To enhance the quality of the data set, for each source we used only the RV measured from the central spaxel (with the largest S/N). By comparing the values obtained from repeated observations of the same stars (which are available especially in the HR fields) and the average RVs of each field, we verified that no relevant offsets in the RV zero-points are present, the average differences being about 2 km s^{-1}, which is consistent with the value of the standard deviation. Hence, the final RV catalog has been generated by averaging the values measured in different data cubes in case of multiple exposures of the same star, using the estimated errors as weights. If a star was sampled both in an HR pointing and in an LR pointing, we kept the value measured in the former for the higher spatial resolution of this instrumental setup.

As discussed below, to reliably investigate the internal kinematics of NGC 6440, we restricted the sample of RVs to the safest measures only. The SINFONI data sample the cluster core where stellar crowding is critical, but the procedure used to extract the spectra includes no source deblending algorithms. Hence, the derived RVs might be affected by the presence of

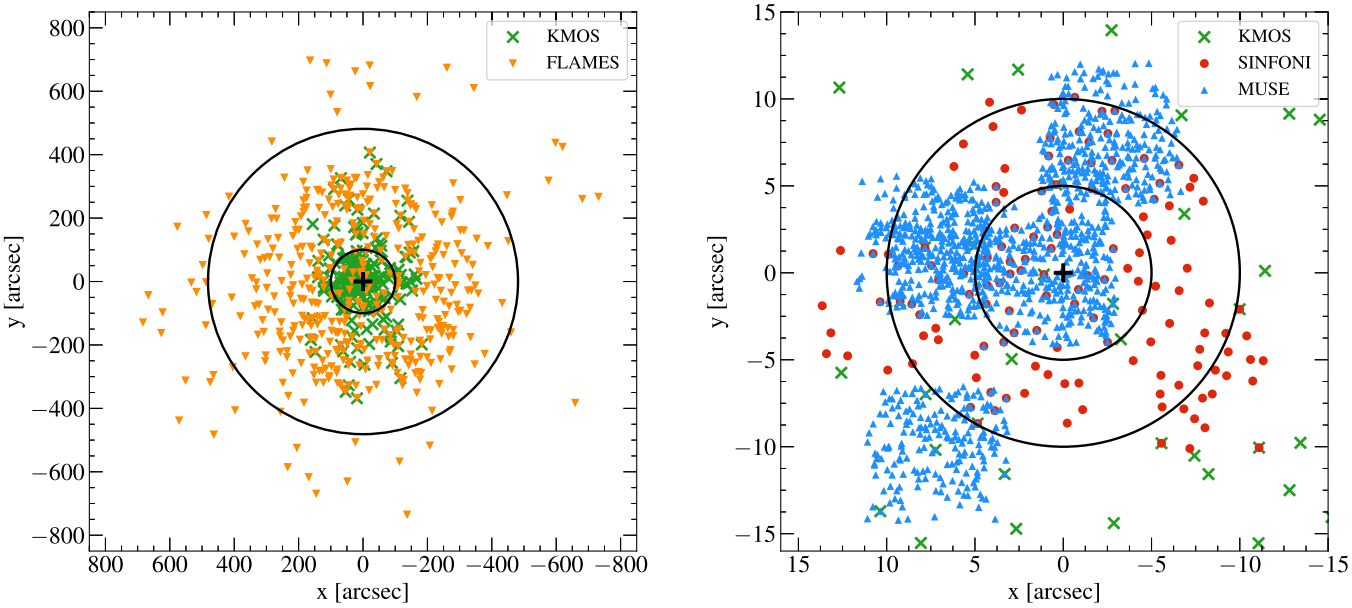

Figure 5. Maps on the plane of the sky, with respect to the adopted cluster center (black plus sign), of the stars with measured RV for each data set. The left panel shows the external portion of the cluster sampled by the FLAMES (orange triangles) and the KMOS (green crosses) data sets. The two circles mark distances of 100″ and 481.″4 (corresponding to the truncation radius of the cluster; see Pallanca et al. 2021) from the center. The right panel is focused on the central region covered by the MUSE (blue triangles) and SINFONI (red circles) samples. A few KMOS targets are also visible (green crosses). The two circles mark distances of 5″ and 10″ from the center.

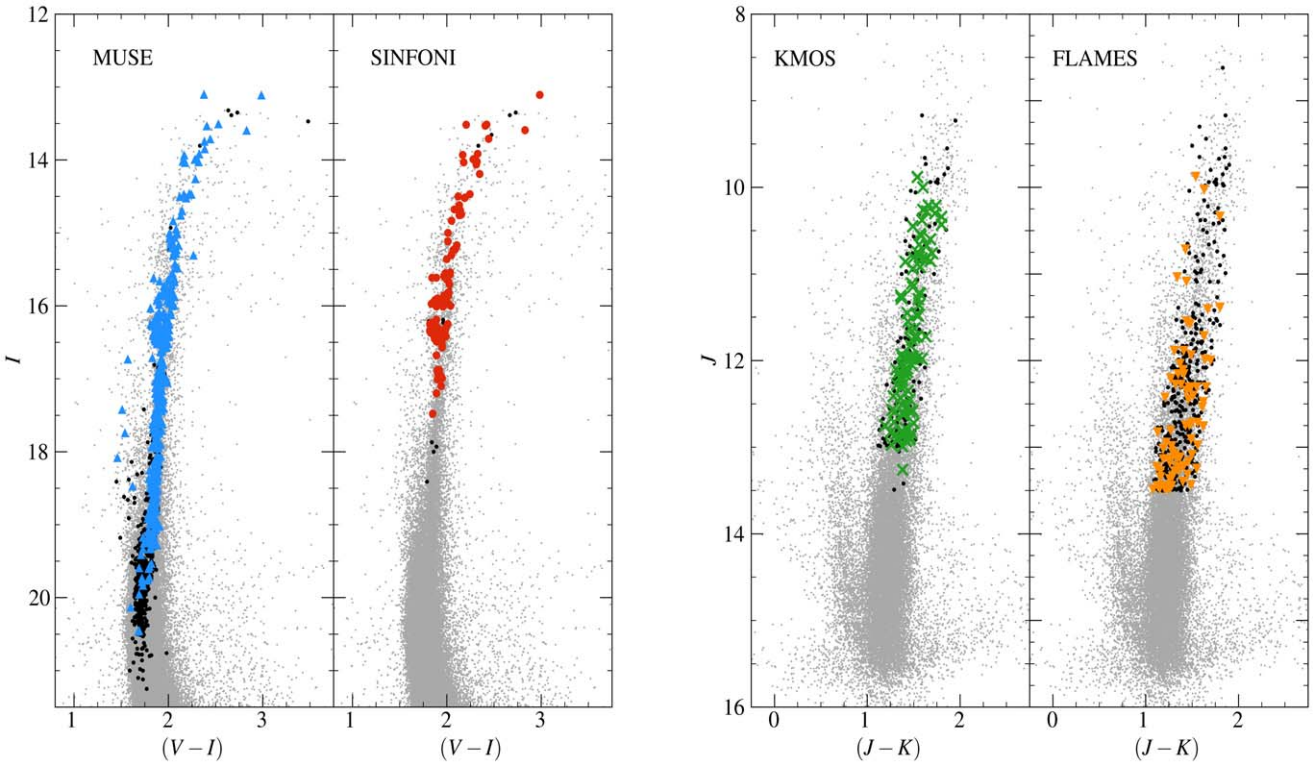

Figure 6. CMDs of NGC 6440, with the star having measured RV highlighted. Left panels: the gray circles show the (I, $V-I$) CMD obtained from the photometric catalog discussed in Pallanca et al. (2021), overplotted with the MUSE (left) and SINFONI (right) samples. The blue triangles on the left and the red circles on the right mark, respectively, the MUSE and SINFONI targets after all the membership and quality selections described in Sections 3.5 and 4, respectively, while the black circles are the rejected targets. Right panels: (J, $J-K$) CMD obtained from the reference SOFI/2MASS catalog (gray circles in both panels; see Section 2), with the KMOS and FLAMES data sets highlighted on the left and on the right, respectively. The green crosses on the left and the orange triangles on the right correspond to the KMOS and FLAMES samples selected for the kinematic analysis, respectively (see Sections 3.5 and 4). The black circles indicate the rejected stars. Note that in each panel the targets observed by two or more instruments are also included.

brighter neighboring stars, and this can impact the final results in terms of the cluster velocity dispersion and systemic rotation. To address this issue and select only the spectra contributed by the light of individual stars, we applied the procedure described in Leanza et al. (2022), which is briefly summarized here. Using as inputs the list of detected stars from the HST catalog and the PSF model adopted in the SINFONI data reduction, the procedure computes the contamination parameter (C) as the

ratio between the fraction of light contributed by the first contaminant and that of the target under analysis, where the first contaminant is the neighboring source providing the second-largest contribution of light to the central spaxel, after the target itself.

For the final SINFONI sample we selected only the safest targets, with negligible contamination from neighboring sources, by including only the stars with contamination parameter lower than 3% ($C < 0.03$). The final catalog consists of 138 RVs for individual stars located between 1.″1 and 15.″0 from the cluster center (red circles in the right panel of Figure 5), in the magnitude range $13 < I < 18$ (see Table 2). The CMD of the targets is shown in the second panel from the left of Figure 6.

3.3. KMOS and FLAMES Data Sets

The procedures adopted to measure the RVs of the KMOS and FLAMES targets are fully described in Ferraro et al. (2018b, 2018c), where MIKiS is presented. Briefly, for the KMOS observations, the 1D spectra have been extracted manually by visually inspecting each IFU and selecting the most exposed spaxel, which corresponds to the stellar centroid. Then, after correction for heliocentric velocity, both KMOS and FLAMES spectra have been cross-correlated with template spectra following the procedure described in Tonry & Davis (1979), which is implemented in the FXCOR task under the software IRAF. To verify that using two different methods does not introduce systematic effects in the RV measurements, we applied the cross-correlation of IRAF to the MUSE spectra, obtaining results in perfect agreement with those obtained with the method described in Section 3.1. As in the cases of the other data sets, the template spectra have been computed with the SYNTHE code (Sbordone et al. 2004; Kurucz 2005) in the appropriate wavelength range, adopting the cluster metallicity and RGB atmospheric parameters and applying a convolution with a Gaussian profile to reproduce the instrument spectral resolutions. For KMOS observations, the RV has been obtained from the cross-correlation with individual near-IR features in the sampled wavelength range, and the RV uncertainties have been derived using Monte Carlo simulations similar to those used for MUSE and SINFONI. For the FLAMES targets, the RV has been measured in three different regions of the spectrum, each including a large number of atomic lines, and the final value and its uncertainty have been obtained, respectively, as the average of the three measures and their dispersion divided by the square root of 3. The typical RV errors are of the order of 1–5 km s^{-1} for the KMOS targets, while they decrease to ∼0.1–0.3 km s^{-1} for the FLAMES measures (bottom right and top right panels of Figure 4, respectively). The final KMOS and FLAMES samples consist of 258 and 448 RV measures, respectively (see Table 2). The left panel of Figure 5 shows the position of the stars on the plane of the sky, with orange triangles and green crosses for the FLAMES and KMOS samples, respectively, while the corresponding CMDs are shown in the third (KMOS) and fourth panels (FLMAES) from the left of Figure 6.

3.4. Final Combined Catalog

Before combining all the RV measurements in a single final catalog, we have checked for possible systematic offsets among the different catalogs. These could be due to the different instrumental setups, including the wavelength range used to derive the RVs, and also the different spectral resolution of each spectrograph.

To this aim, we compared the RVs of the stars in common between two data sets, using only reliable RV measures (i.e., high S/N and small RV uncertainty) and adopting the values obtained from the FLAMES observations as a reference, due to the highest spectral resolution of this instrument. From the stars in common between FLAMES and KMOS, we found an average offset of −5.2 km s^{-1}, which was then applied to the KMOS measures for realigning this sample with the reference one. Unfortunately, no stars are in common between the FLAMES data set and the MUSE and SINFONI ones, since they sample very different regions of the cluster. Moreover, no reliable enough RV measures from the KMOS observations have been found in common with the MUSE and SINFONI data sets. Therefore, to realign the innermost samples with the reference catalog, we compared, after excluding the obvious outliers, the average velocities obtained from the FLAMES and the MUSE catalogs, finding a good agreement within the errors (-67.5 ± 1.1 km s^{-1} and -67.7 ± 0.5 km s^{-1}, respectively). As a last step, a very small residual offset of −1.0 km s^{-1} was detected between the RVs of the stars in common between the MUSE and the SINFONI data sets. Hence, this offset was applied to the SINFONI RVs to realign this sample with all other catalogs.

To create the final catalog, we combined the four data sets (summarized in Table 2) by performing a weighted mean of the RV measures by using the individual errors as weights, for the targets observed by more than one instrument. The final catalog consists of 1831 RV measurements of individual stars,[7] sampling the entire radial extension of the cluster, from 0.″1 out to 778″ (corresponding to ∼1.6 times the truncation radius $r_t = 481.''4$, and ∼15 times the three-dimensional half-mass radius $r_h = 50.''2$; see Pallanca et al. 2021) from the cluster center, as shown in Figure 5, and covering a wide magnitude range ($13 < I < 22$; see Figure 6).

3.5. Cluster Membership

Being a GC in the bulge direction, the contamination from field stars of the population of NGC 6440 is not negligible. For this reason, a thoughtful and accurate analysis was performed to properly address the issue of cluster membership of the measured stars. For the external sample (FLAMES and KMOS), we took advantage of the PMs provided in the Gaia EDR3 (Gaia Collaboration et al. 2021): we selected as cluster members the stars with PMs within 0.9 mas yr^{-1} from the absolute motion of NGC 6440 (Vasiliev & Baumgardt 2021) in the vector-point diagram (VPD; see the top left panel of Figure 7), this value corresponding to ∼3 times the central velocity dispersion of NGC 6440 (see Section 4.2), assuming a distance of 8.3 kpc (Pallanca et al. 2021). The same could not be done for the internal sample (mostly MUSE and SINFONI) because either they have no measured PM or the measures are not reliable, due to the limited capabilities of Gaia in the very central regions of dense GCs like NGC 6440. Therefore, to identify the cluster members in the innermost samples, we used the same criteria based on the relative HST PMs presented in

[7] The final catalog, including the identification number, R.A., decl., RV measure, and its error for each star, is available for free download at http://www.cosmic-lab.eu/Cosmic-Lab/MIKiS_Survey.html.

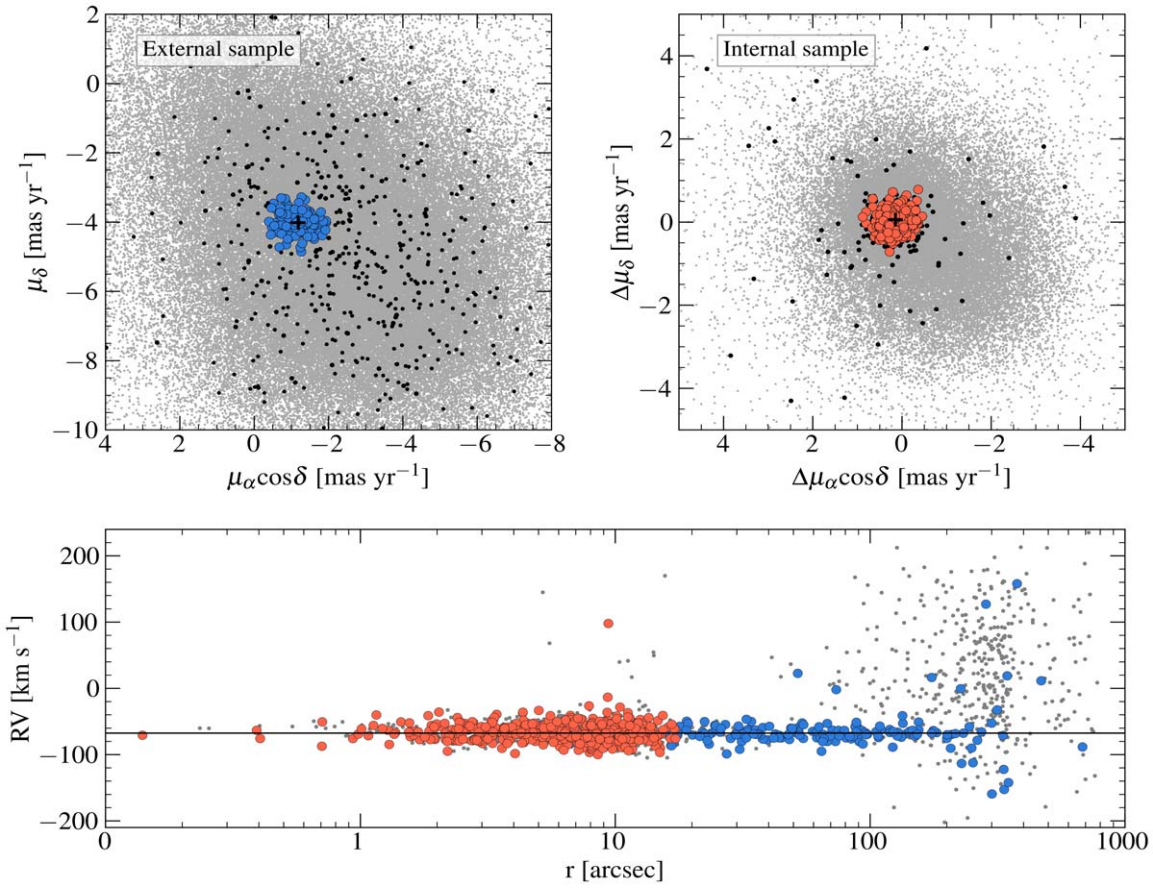

Figure 7. Top left panel: VPD of the Gaia EDR3 data set (gray circles), with the targets of the external sample selected as member stars marked with blue circles. The black circles show the targets rejected as field stars. The black plus sign marks the absolute motion of NGC 6440 (Vasiliev & Baumgardt 2021). Top right panel: VPD of the relative HST PMs obtained in Pallanca et al. (2019; gray circles). The red circles mark the member stars selected from the internal sample, while the black circles are the targets considered as nonmember stars. Bottom panel: RVs of the final catalog as a function of the distance from the cluster center. The large circles show the targets selected as cluster members, color-coded as in the top panels. The targets rejected as field stars are marked with gray circles.

Pallanca et al. (2019). The VPD and the member selection of the internal sample are shown in the top right panel of Figure 7. The bottom panel of the figure shows the measured RVs as a function of the distance from the center, with the PM-selected member stars highlighted as large colored circles. As is apparent, the RVs of the bulk of cluster members are centered at about -67 km s^{-1}, while field stars have significantly different (especially larger) RVs and become dominant in the most external regions. The residual field contamination that appears to be still present in the PM-selected sample, especially at large distances from the center, will be easily removed in the following analysis by means of a σ-clipping procedure aimed at excluding the obvious outliers (see Section 4).

4. Results

To properly explore the internal kinematics of NGC 6440, in the following analysis we have used only stars with the most reliable RV measures, selected by adopting the following criteria. Among the PM-selected cluster members, only the targets with S/N $>$ 15 and RV error $<$ 5 km s^{-1} have been considered. After applying these selections to the targets of the combined catalog (see Section 3.4), we obtained a total sample of 704 targets. Figure 6 shows the positions of the selected targets in the appropriate CMDs. This is the sample of RV measurements that we used to determine the systemic velocity and the velocity dispersion profile and to detect possible signatures of rotation.

4.1. Systemic Velocity

The measured RVs as a function of the distance from the center are plotted in the left panel of Figure 8, and the corresponding RV distribution is shown in the right panel. The gray circles and open histogram refer to the entire final catalog (1831 RV measures), and the apparent well-defined peak indicates the cluster systemic velocity ($V_{\rm sys}$). For the measure of $V_{\rm sys}$ only, in order to minimize the risk of a residual contamination from field stars, from the confident sample of stars selected as described above, we considered only those with distances within 200″ ($\sim 4 \times r_h$) from the center and with RVs in the range -92 km s^{-1} $<$ RV $<$ -42 km s^{-1}, and we applied a 3σ-clipping procedure to remove the obvious outliers. The resulting sample of 625 RVs is shown in the left panel of Figure 8 as black circles, while its distribution is plotted as a gray histogram in the right panel. Hence, under the assumption that the RV distribution of the selected stars is Gaussian, the value of $V_{\rm sys}$ and its uncertainty have been computed through a maximum likelihood method (Walker et al. 2006). We obtained $V_{\rm sys} = -67.5 \pm 0.4$ km s^{-1}. This estimate is in good agreement with the previous result published in Baumgardt & Hilker (2018; -67.8 ± 1.0 km s^{-1}), while it disagrees with the value quoted in Harris (1996; -76.6 ± 2.7 km s^{-1}). In the following,

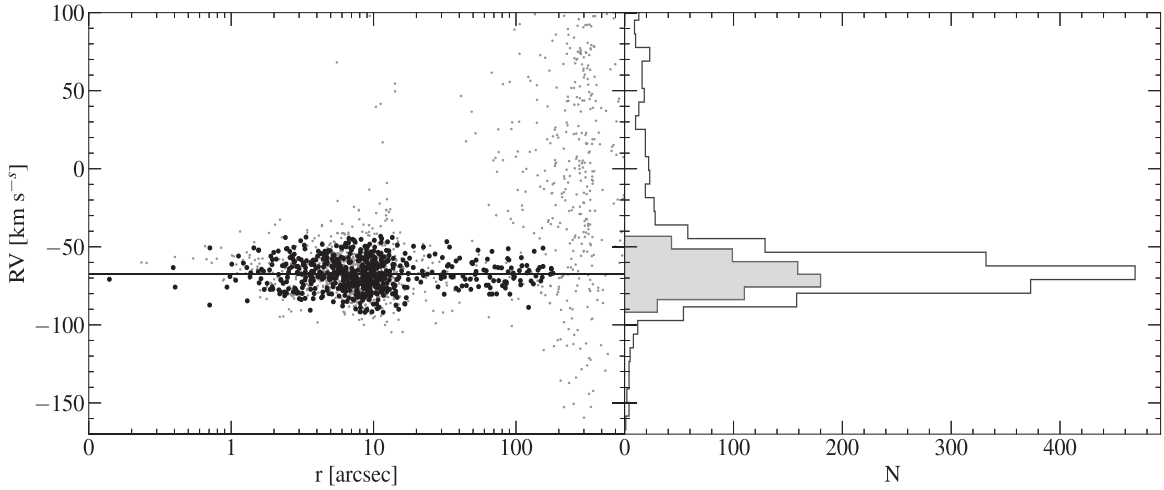

Figure 8. Left panel: RVs of the final catalog (gray circles) as a function of the distance from the cluster center, with the 625 RVs used to determine the cluster systemic velocity (solid line) highlighted as black circles. Right panel: number distributions of the final catalog (open histogram) and of the targets used for the determination of $V_{\rm sys}$ (gray histogram).

we will indicate as $V_r = {\rm RV} - V_{\rm sys}$ the RVs referred to the cluster systemic velocity.

4.2. Second Velocity Moment Profile

As discussed in previous papers (e.g., Lanzoni et al. 2018a; Leanza et al. 2022), the second velocity moment profile ($\sigma_{\rm II}(r)$) derived from the measured RVs represents a very good approximation of the projected velocity dispersion profile $\sigma_P(r)$, in the case of no or negligible systemic rotation, according to the relation

$$\sigma_P^2(r) = \sigma_{\rm II}^2(r) - A_{\rm rot}^2(r), \quad (1)$$

where $A_{\rm rot}$ is the amplitude of the rotation curve. For this cluster no evident signatures of rotation have been clearly detected in previous works. Therefore, we first compute the second velocity moment profile to compare it with the previous results, and then, in Section 4.3, we complete the kinematic analysis of the cluster, investigating the possible presence of internal rotation.

To determine the second velocity moment profile, starting from the RV sample selected as described in Section 4, we have adopted the standard approach already used in previous works (see Ferraro et al. 2018b; Lanzoni et al. 2018a, 2018b; Leanza et al. 2022): the RV sample is divided into radial bins using a set of concentric annuli, which are selected at increasing distance from the cluster center and provide a good compromise between fine radial sampling and statistically significant numbers of stars (at least 30) in each bin. A 3σ-clipping procedure is performed on the RVs in each radial bin to exclude the obvious outliers from the analysis. Then, we applied a maximum likelihood method (Walker et al. 2006; see also Martin et al. 2007; Sollima et al. 2009) to compute the dispersion of the V_r values of the selected stars in each bin. The uncertainties are estimated following the procedure described in Pryor & Meylan (1993).

The resulting $\sigma_{\rm II}(r)$ profile of NGC 6440 is shown in Figure 9 (black circles) and listed in Table 3. It nicely follows the King model (red line) that best fits the observed star density profile of the cluster (Pallanca et al. 2021). We have estimated the central velocity dispersion as the value that minimizes the residuals between the observed velocity dispersion profile and the adopted King model, finding $\sigma_0 = 12.0 \pm 0.4$ km s^{-1}. The 1σ uncertainty has been obtained from the solutions of the χ^2 test for which $\chi^2 = \chi^2_{\rm min} \pm 1$.

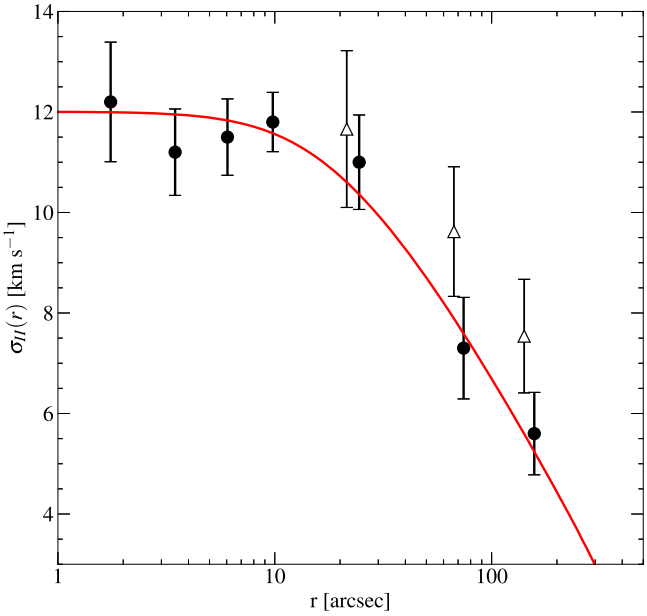

Figure 9. Second velocity moment profile of NGC 6440 obtained from the measured individual RVs (filled circles). The open triangles show the profile derived by Baumgardt & Hilker (2018). The red solid line represents the King model that best fits the star density profile of the cluster (Pallanca et al. 2021).

In Figure 9 we also compare our result with the observed profile obtained by Baumgardt & Hilker (2018; open triangles) from RV measures at intermediate and large radii from the center. Formally, the two outermost points of Baumgardt & Hilker (2018) are larger than ours, possibly due to a different membership selection applied in the two works, or an effect of residual field star contamination in the former. The difference, however, is not significant (the error bars are just 1σ), but we verified that the King model that best fits the observed density distribution would be unable to reproduce a velocity dispersion profile obtained by combining our innermost four points and the three measures by Baumgardt & Hilker (2018), while it is

Table 3
Second Velocity Moment Profiles Obtained for NGC 6440

r_i (arcsec)	r_e (arcsec)	r_m (arcsec)	N	$\sigma_{\rm II}$ (km s^{-1})	$\epsilon_{\sigma_{\rm II}}$ (km s^{-1})
0.01	2.50	1.75	58	12.20	1.19
2.50	4.50	3.47	96	11.20	0.86
4.50	7.50	6.05	130	11.50	0.76
7.50	13.00	9.79	228	11.80	0.59
13.00	50.00	24.49	79	11.00	0.94
50.00	100.00	74.23	37	7.30	1.01
100.00	250.00	157.22	30	5.60	0.82

Note. The first three columns list the internal, external, and mean radii of each adopted radial bin (r_i, r_e, and r_m, respectively), with the mean radius computed as the average distance from the center of all the stars in the bin (N; fourth column). The last two columns list the second velocity moment and its uncertainty in each bin, respectively.

well consistent with the determination provided in this work (filled circles and red line in Figure 9).

4.3. Systemic Rotation

In previous kinematics analysis (e.g., Sollima et al. 2019; Vasiliev & Baumgardt 2021) no unambiguous signals of rotation have been detected in the external regions of NGC 6440. However, thanks to the large sample of MUSE and SINFONI data presented here, we have the opportunity to perform the very first exploration of the central region of the cluster searching for evidence of systemic rotation.

To this purpose, we used the method fully described in previous works (see, e.g., Cote et al. 1995; Lane et al. 2009; Bellazzini et al. 2012; Lanzoni et al. 2013) and adopted in several papers (Bianchini et al. 2013; Boberg et al. 2017; Ferraro et al. 2018c; Lanzoni et al. 2018a, 2018b; Leanza et al. 2022). Following this method, the RV sample is split into two subsamples by a line passing through the cluster center, varying the position angle (PA) of the line from 0° (north direction) to 180° (south direction) by steps of 10°, and with PA = 90° corresponding to the east direction. For each value of PA, the difference between the mean velocity of the two RV subsamples ($\Delta V_{\rm mean}$) is computed. In the presence of systemic rotation, $\Delta V_{\rm mean}$ would show a coherent sinusoidal variation as a function of PA. The maximum/minimum absolute value of this curve provides twice the rotation amplitude ($A_{\rm rot}$) and the PA of the rotation axis ($\rm PA_0$). In addition, if the cluster is rotating, the stellar distribution in a diagram showing the velocity V_r as a function of the projected distances from the rotation axis (XR) shows an asymmetry, with two diagonally opposite quadrants being more populated than the other two. Moreover, the subsamples of stars on each side of the rotation axis are expected to also show different cumulative V_r distributions. Three estimators have been used to quantify the statistical significance of the detected differences: the probability that the RV distributions of the two subsamples are extracted from the same parent family is estimated by means of a Kolmogorov–Smirnov test, while the statistical significance of the difference between the two sample means is evaluated with both the Student's t-test and a maximum likelihood approach.

Of course, by construction, the method can be used only in the case of an RV sampling symmetrically distributed in the plane of the sky. Thus, in order to avoid some heavy undersampled regions, we were forced to limit our analysis to the innermost 5″ portion (approximately covering the core radius of the cluster $r_c = 6\farcs4$; Pallanca et al. 2021), where the combination of the MUSE and SINFONI samples offers a reasonably symmetric coverage of the cluster (see Figure 5). We thus performed the analysis over the entire region ($r < 5''$) and in two radial annuli around the cluster center ($r < 3''$ and $3'' < r < 5''$).

The results are plotted in Figure 10 and listed in Table 4. The diagnostic plots show the characteristics of systemic rotation in the considered regions: a sinusoidal behavior of $\Delta V_{\rm mean}$ as a function of PA (left panels), asymmetric distributions of V_r as a function of XR (middle panels), and well-distinct cumulative V_r distributions for the two samples on either side of the rotation axis (right panels). Hence, we can reasonably (at $\sim 2\sigma$ statistical significance) conclude that the core region within 5″ of NGC 6440 is rotating, with an average PA of the rotation axis $\rm PA_0 \sim 132° \pm 2°$ and an amplitude of $\sim 2.8 \pm 0.2$ km s^{-1}. Unfortunately, the nonuniform coverage of the intermediate region of the cluster does not allow us to assess the exact radial extension of the rotation signal. Moreover, we have searched for signatures of systemic rotation in the outermost part of the cluster by applying the same procedure to the regions covered by KMOS and FLAMES. In this case, no significant evidence of rotation was found, in agreement with previous studies (Sollima et al. 2019; Vasiliev & Baumgardt 2021).

4.4. Ellipticity

From previous analyses, NGC 6440 shows a low global ellipticity (0.01; see Harris 1996), as expected for a nonrotating system. However, because of the rotation signal detected in the core, we have explored the morphology of the innermost region of the cluster to check for a possible flattening of the system in the direction perpendicular to the rotation axis, as expected from theoretical models (e.g., Chandrasekhar 1969; Varri & Bertin 2012). We thus determined the 2D stellar density map of the inner $\sim 50'' \times 50''$ area, by using the stars with $I < 20.5$ (to avoid incompleteness effects) in the photometric catalog of Pallanca et al. (2021). By applying a Gaussian kernel to the stellar distribution (see Dalessandro et al. 2015), we obtained the smoothed 2D surface density map shown in Figure 11. The gray solid lines represent the best-fit ellipses to the isodensity contours and show that the system is slightly flattened in the center and acquires a more spherical symmetry for increasing radii. Indeed, the resulting ellipticity (defined as $\epsilon = 1 - b/a$, with a and b being the major and minor axes, respectively) achieves its maximum value (0.18 ± 0.02) at $r \sim 3''$ and gradually decreases at larger radii ($\epsilon = 0.04 \pm 0.02$ at $r \sim 45''$). Where the ellipticity is maximum, the ellipses' major axis has an orientation of $\sim 15°$ from north to east. Although the direction of the major axis is not exactly perpendicular to the rotation axis ($\rm PA_0 \sim 132° \pm 2°$), the presence and the orientation of the detected flattening are qualitatively consistent with the systemic rotation signal found in the inner 5″ of the system.

5. Discussion and Conclusions

As part of MIKiS (Ferraro et al. 2018b, 2018c), here we presented the velocity dispersion profile and the detection of a core rotation for the bulge GC NGC 6440. Thanks to a combination of different spectroscopic data sets acquired with

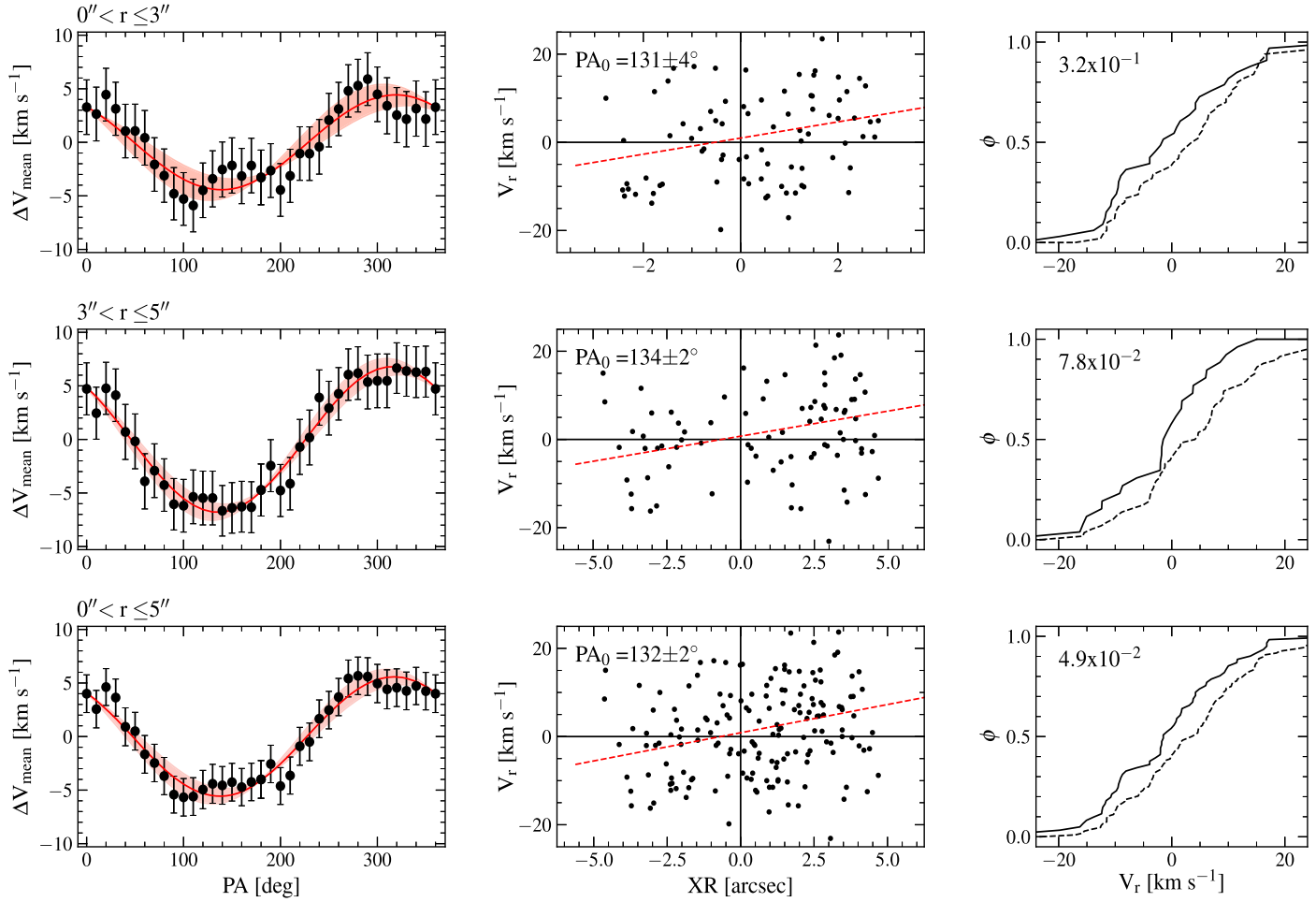

Figure 10. Diagnostic diagrams of the rotation signature detected in three concentric radial bins in the core of the cluster at different distances from the center (see labels in the upper left corner of each row). For each bin, the left panels show the difference between the mean RV on each side of a line passing through the center with a given PA, as a function of PA itself. The solid line is the sine function that best fits the observed patterns, and the red shaded region marks the confidence level at 3σ. The middle panels show the distribution of the velocities V_r as a function of the projected distances from the rotation axis (XR) in arcseconds. The value of PA_0 is labeled in each panel. The red dashed lines are the least-squares fits the data. The right panels show the cumulative V_r distributions for the stars with XR <0 (solid line) and for those with XR >0 (dotted line). The Kolmogorov–Smirnov probability that the two samples are extracted from the same parent distribution is also labeled.

Table 4
Rotation Signature Detected in the Core of NGC 6440 in Three Circular Annuli around the Cluster Center

r_i	r_e	r_m	N	PA_0	A_{rot}	P_{KS}	P_{Stud}	n-σ_{ML}
0.01	3.00	2.10	85	131 ± 4	2.2 ± 0.3	3.2×10^{-1}	<90.0	2.2
3.00	5.00	3.90	86	134 ± 2	3.4 ± 0.3	7.8×10^{-2}	>95.0	3.3
0.01	5.00	3.00	171	132 ± 2	2.8 ± 0.2	4.9×10^{-2}	>95.0	3.6

Note. The table lists inner (r_i), outer (r_e) and mean radius (r_m) in arcseconds, the number of stars in the bin (N), the PA of the rotation axis (PA_0) and its 1σ error in degree, the rotation amplitude (A_{rot}) and its error in km s^{-1}, the Kolmogorov–Smirnov probability that the two samples on each side of the rotation axis are drawn from the same parent distribution (P_{KS}), the t-Student probability that the two RV samples have different means (P_{Stud}), and the significance level (in units of n-σ) that the two means are different following a maximum likelihood approach (n-σ_{ML}).

appropriate spatial resolution, we measured the RV of ∼1800 individual stars sampling the entire radial extension, beyond r_t of the cluster. Using only the sample of member stars properly selected with the most reliable RV measures, we have derived the velocity dispersion profile of the system from its innermost (∼0.″1) to the outer regions of the cluster (∼250″), covering about $5 \times r_h$ from the center. We also detected a rotation signal in the innermost ∼5″ of the cluster, while no conclusions can be drawn for larger distances because of a nonhomogeneous sampling of the more external areas.

The present work complements the detailed photometric study of the cluster recently performed by our group (Pallanca et al. 2019, 2021), which provided high-resolution extinction maps in the direction of the cluster, a new determination of the average reddening, a new star density profile, and updated values of the structural parameters, distance modulus, and age of the cluster. Adopting some of these quantities and the resulting value of σ_0 (12.0 ± 0.4 km s^{-1}; see Section 4.2), we have verified that the adopted King model reproduces reasonably well also the velocity dispersion profile of the cluster (see Figure 9).

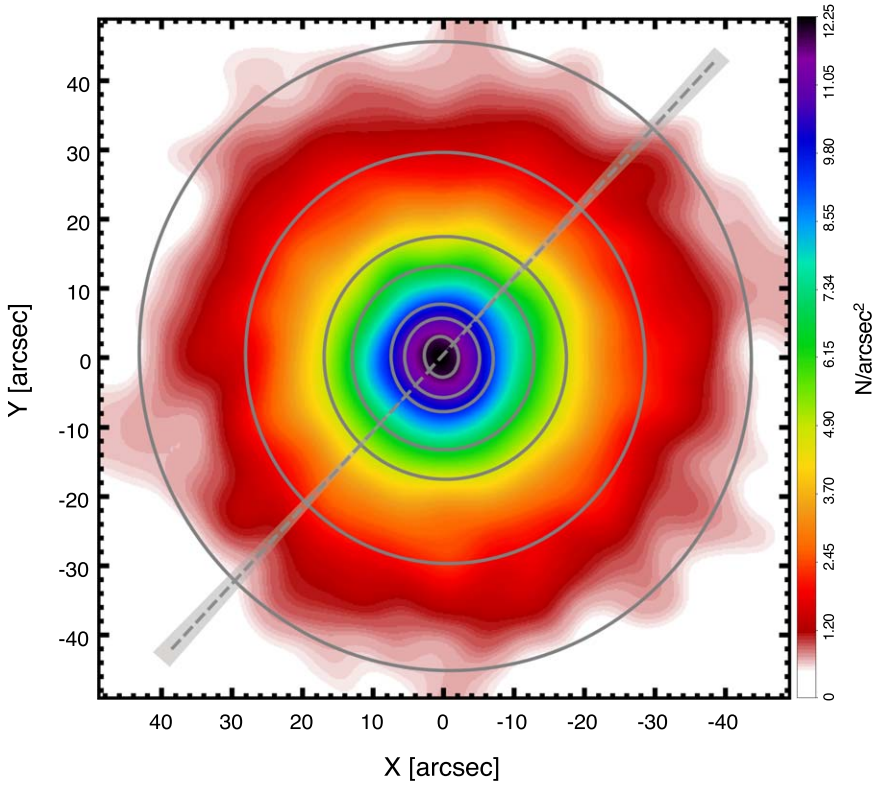

Figure 11. Projected stellar density map of the central region of NGC 6440. The solid gray lines are the best-fit ellipses to the isodensity curves, and the gray dashed line marks the estimated direction of the rotation axis ($PA_0 \sim 132^\circ \pm 2^\circ$; see Section 4.3), with the 1σ error shown by the shaded area.

Compared to Baumgardt & Hilker (2018), our profile samples a much more inner region of the cluster, and our estimate of σ_0 is significantly smaller (12 km s^{-1}, in place of 15.8 km s^{-1}). This difference could be ascribed to an effect of energy equipartition and mass segregation, which implies a lower velocity dispersion for RGB stars, compared to the average, less massive, cluster members. Indeed, based on its age and current half-mass relaxation time ($t = 13$ Gyr and $t_{rh} = 1$ Gyr, respectively; Pallanca et al. 2021; see also Baumgardt & Hilker 2018), NGC 6440 has undergone about 13 relaxations so far, and it is likely mass segregated. Consistently, the value of σ_0 estimated in this work (which has been obtained mainly from giant stars) is smaller than the mass-weighted central velocity dispersion determined by Baumgardt & Hilker (2018) from the comparison with *N*-body simulations.

According to Equation (1), in the presence of rotation, the velocity dispersion is expected to be smaller than the second velocity moment. However, in the case of NGC 6440 the contribution of the detected rotation signal is small compared to the measured second velocity moment; thus, we can conclude that the cluster is, with a reasonable approximation, a pressure-supported system, dominated by nonordered motions. These considerations make the approximation that the cluster is well represented by single-mass, spherical, isotropic, and nonrotating (King 1966) models well acceptable. Hence, we can use the derived value of σ_0 to estimate the total mass of the system. To this end, we used Equation (3) of Majewski et al. (2003), deriving μ as in Djorgovski (1993) and assuming $\beta = 1/\sigma_0^2$ (see Richstone & Tremaine 1986). We then estimated the total mass uncertainty by running 1000 Monte Carlo simulations, extracting the values of c, r_0, and σ_0 from an appropriate normal distribution for each parameter (see Leanza et al. 2022). The result obtained for NGC 6440 is $M = 2.66^{+0.27}_{-0.24} \times 10^5\ M_\odot$. We emphasize, however, that this value likely underestimates the true total mass of the system because the adopted central velocity dispersion has been measured from giant stars (see above). This is qualitatively in agreement with the larger mass ($(4.42 \pm 0.64) \times 10^5\ M_\odot$) estimated by Baumgardt & Hilker (2018) from the mass-weighted value of σ_0.

Although no evidence of systemic rotation has been detected in previous analyses (see Sollima et al. 2019; Vasiliev & Baumgardt 2021), and although in the present work we could not derive a rotation curve for reasons of nonuniform sampling, a nonnegligible signal of ordered rotation has been found in the core of NGC 6440 (see Section 4.3). By assuming that the maximum peak of the rotation is $\sim 3.4 \pm 0.3$ km s^{-1} between $3''$ and $5''$ from the center, as found in the present work, we can derive the value of $V_{\rm rot}/\sigma_0 = 0.3$, similarly to what has been done in other works (Bianchini et al. 2013; Fabricius et al. 2014; Boberg et al. 2017; Dalessandro et al. 2021). Nevertheless, since the nonuniform sampling prevents the exploration of the rotation signal at larger radii, we cannot exclude that the rotation peak is higher for $r > 5''$. Despite this, it is interesting to note that such a central rotation is a rare feature in GCs and only two similar cases are known to date in the literature, namely M15 (van den Bosch et al. 2006; Usher et al. 2021) and NGC 6362 (Dalessandro et al. 2021). Interestingly, *N*-body simulations (Tiongco et al. 2017) show that such central ($<r_h$) velocity signals are expected only in very dynamically evolved systems that lost a significant amount of their mass because of both two-body relaxation effects and interactions with the host galaxy potential. However, we stress that this result deserves further investigation and additional

analysis at larger radii to see whether the rotation signal extends beyond the core region.

S.L. warmly thanks S. Kamann for useful suggestions about PampelMuse. E.V. acknowledges the Excellence Cluster ORIGINS Funded by the Deutsche Forschungsgemeinschaft (DFG, German Research Foundation) under Germany's Excellence StrategyEXC-2094390783311. This work is part of the project Cosmic-Lab at the Physics and Astronomy Department "A. Righi" of the Bologna University (http://www.cosmic-lab.eu/ Cosmic-Lab/Home.html). The research was funded by the MIUR through the PRIN-2017 grant awarded to the project Light-on-Dark (PI:Ferraro) with contract PRIN-2017K7REXT.

ORCID iDs

Silvia Leanza https://orcid.org/0000-0001-9545-5291
Cristina Pallanca https://orcid.org/0000-0002-7104-2107
Francesco R. Ferraro https://orcid.org/0000-0002-2165-8528
Barbara Lanzoni https://orcid.org/0000-0001-5613-4938
Emanuele Dalessandro https://orcid.org/0000-0003-4237-4601
Mario Cadelano https://orcid.org/0000-0002-5038-3914
Enrico Vesperini https://orcid.org/0000-0003-2742-6872
Livia Origlia https://orcid.org/0000-0002-6040-5849
Alessio Mucciarelli https://orcid.org/0000-0001-9158-8580
Elena Valenti https://orcid.org/0000-0002-6092-7145

References

Anderson, J., & King, I. R. 2006, Instrument Science Report ACS, 2006–01, 34
Arsenault, R., Madec, P.-Y., Hubin, N., et al. 2008, Proc. SPIE, 7015, 701524
Bacon, R., Accardo, M., Adjali, L., et al. 2010, Proc. SPIE, 7735, 773508
Bailyn, C. D. 1995, ARA&A, 33, 133
Baumgardt, H., & Hilker, M. 2018, MNRAS, 478, 1520
Bellazzini, M., Bragaglia, A., Carretta, E., et al. 2012, A&A, 538, A18
Bianchini, P., Varri, A. L., Bertin, G., et al. 2013, ApJ, 772, 67
Boberg, O. M., Vesperini, E., Friel, E. D., et al. 2017, ApJ, 841, 114
Cadelano, M., Chen, J., Pallanca, C., et al. 2020, ApJ, 905, 63
Cadelano, M., Dalessandro, E., Ferraro, F. R., et al. 2017b, ApJ, 836, 170
Cadelano, M., Ferraro, F. R., Istrate, A. G., et al. 2019, ApJ, 875, 25
Cadelano, M., Pallanca, C., Ferraro, F. R., et al. 2017a, ApJ, 844, 53
Cadelano, M., Ransom, S. M., Freire, P. C. C., et al. 2018, ApJ, 855, 125
Cadelano, M., Saracino, S., Dalessandro, E., et al. 2020a, ApJ, 895, 54
Chandrasekhar, S. 1969, ApJ, 157, 1419
Cote, P., Welch, D. L., Fischer, P., et al. 1995, ApJ, 454, 788
Djorgovski, S. 1993, ASP Conf. Ser. 50, Structure and Dynamics of Globular Clusters, ed. S. G. Djorgovski & G. Meylan (San Francisco, CA: ASP), 373
Dalessandro, E., Miocchi, P., Carraro, G., Jilkova, L., & Moitinho, A. 2015, MNRAS, 449, 1811
Dalessandro, E., Raso, S., Kamann, S., et al. 2021, MNRAS, 506, 813
Dalessandro, E., Ferraro, F. R., & Bastian, N. 2019, A&A, 621, A45
Eisenhauer, F., Abuter, R., Bickert, K., et al. 2003, Proc. SPIE, 4841, 1548
Fabricius, M. H., Noyola, E., Rukdee, S., et al. 2014, ApJL, 787, L26
Ferraro, F. R., Beccari, G., Dalessandro, E., et al. 2009a, Natur, 462, 1028
Ferraro, F. R., Dalessandro, E., Mucciarelli, A., et al. 2009b, Natur, 462, 483
Ferraro, F. R., Lanzoni, B., Dalessandro, E., et al. 2012, Natur, 492, 393
Ferraro, F. R., Lanzoni, B., Dalessandro, E., et al. 2019, NatAs, 3, 149
Ferraro, F. R., Lanzoni, B., Raso, S., et al. 2018a, ApJ, 860, 36
Ferraro, F. R., Massari, D., Dalessandro, E., et al. 2016, ApJ, 828, 75
Ferraro, F. R., Mucciarelli, A., Lanzoni, B., et al. 2018b, ApJ, 860, 50
Ferraro, F. R., Mucciarelli, A., Lanzoni, B., et al. 2018c, Msngr, 172, 18
Ferraro, F. R., Pallanca, C., Lanzoni, B., et al. 2015, ApJL, 807, L1
Ferraro, F. R., Pallanca, C., Lanzoni, B., et al. 2021, NatAs, 5, 311
Fétick, R. J. L., Fusco, T., Neichel, B., et al. 2019, A&A, 628, A99
Freudling, W., Romaniello, M., Bramich, D. M., et al. 2013, A&A, 559, A96
Gaia Collaboration, Brown, A. G. A., Vallenari, A., et al. 2021, A&A, 649, A1
Giersz, M., Leigh, N., Hypki, A., Lutzgendorf, N., & Askar, A. 2015, MNRAS, 454, 3150
Gottgens, F., Kamann, S., Baumgardt, H., et al. 2021, MNRAS, 507, 4788
Harris, W. E. 1996, AJ, 112, 1487
Kamann, S., Wisotzki, L., & Roth, M. M. 2013, A&A, 549, A71
King, I. R. 1966, AJ, 71, 64
Kurucz, R. L. 2005, MSAIS, 8, 14
Lane, R. R., Kiss, L. L., Lewis, G. F., et al. 2009, MNRAS, 400, 917
Lanzoni, B., Dalessandro, E., Ferraro, F. R., et al. 2007, ApJL, 668, L139
Lanzoni, B., Ferraro, F. R., Alessandrini, E., et al. 2016, ApJL, 833, L29
Lanzoni, B., Ferraro, F. R., Dalessandro, E., et al. 2010, ApJ, 717, 653
Lanzoni, B., Ferraro, F. R., Dalessandro, E., et al. 2019, ApJ, 887, 176
Lanzoni, B., Ferraro, F. R., Mucciarelli, A., et al. 2018a, ApJ, 861, 16
Lanzoni, B., Ferraro, F. R., Mucciarelli, A., et al. 2018b, ApJ, 865, 11
Lanzoni, B., Mucciarelli, A., Origlia, L., et al. 2013, ApJ, 769, 107
Leanza, S., Pallanca, C., Ferraro, F. R., et al. 2022, ApJ, 929, 186
Magorrian, J., Tremaine, S., Richstone, D., et al. 1998, AJ, 115, 2285
Majewski, S. R., Skrutskie, M. F., Weinberg, M. D., et al. 2003, ApJ, 599, 1082
Martin, N. F., Ibata, R. A., Chapman, S. C., Irwin, M., & Lewis, G. F. 2007, MNRAS, 380, 281
Mauro, F., Moni Bidin, C., Cohen, R., et al. 2012, ApJL, 761, L29
Miocchi, P., Lanzoni, B., Ferraro, F. R., et al. 2013, ApJ, 774, 151
Origlia, L., Ferraro, F. R., Fusi Pecci, F., et al. 1997, A&A, 321, 859
Origlia, L., Valenti, E., & Rich, R. M. 2008, MNRAS, 388, 1419
Pallanca, C., Beccari, G., Ferraro, F. R., et al. 2017, ApJ, 845, 4
Pallanca, C., Dalessandro, E., Ferraro, F. R., et al. 2010, ApJ, 725, 1165
Pallanca, C., Dalessandro, E., Ferraro, F. R., et al. 2013, ApJ, 773, 122
Pallanca, C., Ferraro, F. R., Lanzoni, B., et al. 2019, ApJ, 882, 159
Pallanca, C., Lanzoni, B., Ferraro, F. R., et al. 2021, ApJ, 913, 137
Pallanca, C., Ransom, S. M., Ferraro, F. R., et al. 2014, ApJ, 795, 29
Pasquini, L., Avila, G., Blecha, A., et al. 2002, Msngr, 110, 1
Pooley, D., Lewin, W. H. G., Anderson, S. F., et al. 2003, ApJL, 591, L131
Portegies Zwart, S. F., Baumgardt, H., Hut, P., et al. 2004, Natur, 428, 724
Pryor, C., & Meylan, G. 1993, ASP Conf. Ser. 50, Structure and Dynamics of Globular Clusters, ed. S. G. Djorgovski & G. Meylan (San Francisco, CA: ASP), 357
Ransom, S. M., Hessels, J. W. T., Stairs, I. H., et al. 2005, Sci, 307, 892
Raso, S., Libralato, M., Bellini, A., et al. 2020, ApJ, 895, 15
Richstone, D. O., & Tremaine, S. 1986, AJ, 92, 72
Sbordone, L., Bonifacio, P., Castelli, F., et al. 2004, MSAIS, 5, 93
Sharples, R., Bender, R., Agudo Berbel, A., et al. 2013, Msngr, 151, 21
Sollima, A., Baumgardt, H., & Hilker, M. 2019, MNRAS, 485, 1460
Sollima, A., Bellazzini, M., Smart, R. L., et al. 2009, MNRAS, 396, 2183
Ströbele, S., La Penna, P., Arsenault, R., et al. 2012, Proc. SPIE, 8447, 844737
Tiongco, M. A., Vesperini, E., & Varri, A. L. 2017, MNRAS, 469, 683
Tonry, J., & Davis, M. 1979, AJ, 84, 1511
Usher, C., Kamann, S., Gieles, M., et al. 2021, MNRAS, 503, 1680
Valenti, E., Ferraro, F. R., & Origlia, L. 2004, MNRAS, 351, 1204
Valenti, E., Ferraro, F. R., & Origlia, L. 2007, AJ, 133, 1287
van den Bosch, R., de Zeeuw, T., Gebhardt, K., et al. 2006, ApJ, 641, 852
Varri, A. L., & Bertin, G. 2012, A&A, 540, A94
Vasiliev, E., & Baumgardt, H. 2021, MNRAS, 505, 5978
Walker, M. G., Mateo, M., Olszewski, E. W., et al. 2006, AJ, 131, 2114
Weilbacher, P. M., Palsa, R., Streicher, O., et al. 2020, A&A, 641, A28